

See discussions, stats, and author profiles for this publication at: <https://www.researchgate.net/publication/229022257>

# Mapping ground deformation by Radar interferometry based on permanent-scatterer network: algorithm and testing results

Article · January 2008

CITATIONS

2

READS

57

5 authors, including:



[Sean Buckley](#)

NASA

36 PUBLICATIONS 338 CITATIONS

[SEE PROFILE](#)



[Xiaoli Ding](#)

The Hong Kong Polytechnic University

296 PUBLICATIONS 3,830 CITATIONS

[SEE PROFILE](#)

# MAPPING GROUND DEFORMATION BY RADAR INTERFEROMETRY BASED ON PERMANENT-SCATTERER NETWORK: ALGORITHM AND TESTING RESULTS

Guoxiang Liu<sup>a,\*</sup>, S. M. Buckley<sup>b</sup>, Xiaoli Ding<sup>c</sup>, Qiang Chen<sup>a</sup>, Xiaojun Luo<sup>a</sup>

<sup>a</sup>Dept. of Surveying Engineering, Southwest Jiaotong University, Chengdu, China - rsgxliu@swjtu.edu.cn

<sup>b</sup>Centre for Space Research, The University of Texas at Austin, Austin, Texas, USA - sean.buckley@mail.utexas.edu

<sup>c</sup>Dept. of Land Surveying and Geo-Informatics, The Hong Kong Polytechnic University, Hong Kong, China -  
lsxlding@polyu.edu.hk

**KEY WORDS:** Ground Deformation, Radar Interferometry, PS Networking, Atmospheric Signal, Empirical Mode Decomposition

## ABSTRACT:

The full operational capability of synthetic aperture radar (SAR) interferometry in deformation monitoring has not been achieved yet due to the negative influences of spatio-temporal decorrelation and atmospheric delay. With the use of time series of SAR images, deformation extraction can be however improved by only tracking some objects with steady radar reflectivity, generally referred to as permanent scatterer (PS). This paper presents an attempt to explore a PS-networking approach to isolate deformations from other effects such as atmospheric signals and topographic errors. The deforming process in time and space is modelled and estimated with a very strong network which is formed by connecting adjacent PSs. The linear deformations and topographic errors are estimated by optimizing objective functions and by adjusting the network via weighted least squares (LS) solution. The time series of nonlinear deformations and atmospheric signals are computed by singular value decomposition (SVD) and empirical mode decomposition (EMD). To validate the algorithm, 39 ERS C-band SAR images acquired over Phoenix in Arizona (USA) from 1992 to 2002 are used to detect land subsidence caused by the excessive groundwater withdrawal.

## 1. INTRODUCTION

Existing studies have shown that there are two major limitations in conventional differential SAR interferometry (DInSAR) for land deformation monitoring, i.e., spatio-temporal decorrelation and atmospheric artifacts (e.g., Zebker & Villaseno, 1992; Buckley, 2000; Liu, 2003; Ding *et al.*, 2004). To mitigate such drawbacks, many research efforts have been made in recent years to explore various techniques for detecting the temporal evolution of deformations using time series of SAR images.

A strategy proposed early is to stack the multiple interferograms (Sandwell & Price, 1998). Ground deformation analysis can be therefore improved by enhancing fringe clarity and suppressing atmospheric effects. Afterwards, a very generic approach, called permanent scatterers (PS) technique, was proposed to extract both linear and nonlinear deformations from a set of interferograms by isolating atmospheric effects and topographic errors (Ferretti *et al.*, 2000, 2001). Since PSs are usually some hard objects such as buildings and rocks, they can remain temporal coherent radar reflectivity, and thus facilitating deformation extraction on the basis of PSs' phase measurements with high signal-to-noise ratio (SNR). Subsequently, another effective approach, called small-baseline subset (SBAS) method, was developed to further decrease the negative influences due to decorrelation noise and bias (Berardino *et al.* 2002).

PS technique suffers from spatial decorrelation as some long-spatial baselines may result in by sharing a unique master image in forming interferometric combinations, while SBAS technique suffers from errors caused by full-resolution phase unwrapping. However, the two techniques can complement each other (Mora *et al.* 2003). Combining the merits of PS and SBAS technique, this paper presents an improved algorithm to isolate and extract

deformations, topographic errors and atmospheric signals with a very strong network formed by freely connecting neighbouring PSs. To maximize coherence of all the SAR dataset, the spatial and temporal baseline thresholding are applied when forming interferometric combinations. The phase modelling is based on the network. The linear deformation velocities and topographic errors are first estimated by optimizing an objective function of each arc (a connection of two PSs) and adjusting the network by LS solution. Time series of phase measurements at each PS is then reconstructed by singular value decomposition (SVD) and decoupled into nonlinear deformations and atmospheric signals by a relatively new signal analysis method - empirical mode decomposition (EMD), proposed by Huang *et al.* (1998). For algorithm validation, some experiments have been carried out to analyze subsidence evolution in Phoenix metropolitan with 39 ERS-1/2 C-band (wavelength of 5.6 cm) SAR images acquired 1992 through 2000.

## 2. DATA PREPROCESSING AND PS NETWORKING

### 2.1 Data Preprocessing

Suppose that deformation analysis is based on  $N+1$  SAR images acquired at the ordered times  $(t_0, t_1, \dots, t_N)$  over the same area. An interferometric combination is acceptable if and only if its temporal baseline is below a given threshold (e.g., 4 years) and its spatial baseline is also below a given threshold (e.g., 120 m for ERS SAR). Let us assume that  $M$  interferograms may be formed in this way. Prior to further analysis, several procedures are necessarily performed to compute differential interferograms.

Since co-registering SAR imagery is a key prerequisite for any

---

\* Corresponding author.

change detection, all the SAR images have to be co-registered into the space of the selected reference image by maximizing correlation between SAR acquisitions. As the subsequent PS detection is based on statistical calculation of SAR data, all the SAR amplitude images are calibrated in a similar way as Lyons & Sandwell (2003). The unique radiometric calibration factor of each image is defined and calculated as a ratio of the amplitude of each image (mean of all pixels) to the mean amplitude of the entire dataset. Each SAR amplitude image is divided by this ratio to make comparable brightness between images.

Each initial interferogram is derived by a pixel-wise conjugate multiplication (equivalent to phase differencing) between the master SAR image and the co-registered slave SAR image. In theory, such direct phase difference at each pixel is due to several contributions, i.e., flat-earth trend, topography, ground motion, atmospheric delay and decorrelation noise. To highlight ground deformation, both the precise orbital data and the external digital elevation model (DEM) are utilized to remove flat-earth trend and topographic effects from each initial interferogram, thus resulting in  $M$  differential interferograms. It should be emphasized here that no any filtering is performed during differential processing to maintain independency in phase data.

Let us assume that the available DEM has errors and the ground motion in radar line-of-sight (LOS) direction is of linear and nonlinear accumulation in time. The differential interferometric phase at a pixel from the  $i$ th interferogram can be modelled as,

$$\Phi_i(T_i) = \frac{4\pi}{\lambda \cdot R \cdot \sin \theta} \cdot B_i^\perp \cdot \varepsilon + \frac{4\pi}{\lambda} \cdot T_i \cdot v + \phi_i^{res}(T_i) \quad (1)$$

where  $B_i^\perp$  = spatial (perpendicular) baseline

$T_i$  = temporal baseline (time interval)

$\lambda$  = radar wavelength (5.66 cm for ERS)

$R$  = sensor-target distance

$\theta$  = radar incident angle

$\varepsilon$  = elevation error

$v$  = linear LOS deformation velocity

$\phi_i^{res}$  = residual phase

## 2.2 PS Networking

As PSs will be used to form an observation network similar to a levelling or GPS network, they need to be picked out from the decorrelated pixels or areas. Using time series of the calibrated SAR amplitude data, we basically follow the strategy by Ferretti *et al.* (2001) to identify PS candidates on a pixel-by-pixel basis. Any pixel with amplitude dispersion index (ADI) less than 0.25 is determined as a PS candidate.

After selection of all the PSs, we connect the neighbouring PSs to form a network. It will be seen that such network can provide a good framework for data modelling and parameter estimating by LS method. Unlike a triangular irregular network (TIN) as applied by Mora *et al.* (2003), we freely link the adjacent PSs using a given threshold of Euclidian distance. Any two PSs are connected only if their distance is less than a give threshold (e.g., 1 km). The PS network formed in this way is hereafter referred to as freely-connected network (FCN).

It should be pointed out that any regionalized variable follows a fundamental geographic principal; that is the samples that are spatially closer together tend to be more alike than those that are farther apart. The concept of neighbourhood differencing is hence often employed to compensate some spatially correlated errors or offsets. Differential GPS is a good example. Likewise, our FCN strategy benefits deformation analysis via differencing operation along each connection (arc) of two PSs in the FCN as some spatially-correlated errors such as atmospheric effects and other biases may be cancelled out more or less.

## 3. MODELLING AND ESTIMATING

### 3.1 Modelling and estimating with PS Network

As discussed in section 2.2, our data modelling is based on the idea of neighbourhood differencing along each arc of the FCN. For the  $i$ th interferometric pair, the differential interferometric phase increment between two adjacent PSs of each arc can be derived from equation (1) and expressed as,

$$\Delta\Phi_i(T_i) = \frac{4\pi}{\lambda \cdot R \cdot \sin \theta} \cdot \overline{B_i^\perp} \cdot \Delta\varepsilon + \frac{4\pi}{\lambda} \cdot T_i \cdot \Delta v + \Delta\phi_i^{res}(T_i) \quad (2)$$

where  $\overline{B_i^\perp}$  = mean of perpendicular baselines at two PSs

$\overline{R}$  = mean of sensor-target distances

$\overline{\theta}$  = mean of radar incident angles

$\Delta\varepsilon$  = increment of elevation errors

$\Delta v$  = increment of linear LOS deformation velocities

$\Delta\phi_i^{res}$  = increment of residual phases

The increment of residual phases  $\Delta\phi_i^{res}$  can be viewed as a sum of several components, i.e., nonlinear-motion phase increment  $\Delta\phi_i^{nldf}$ , atmospheric phase increment  $\Delta\phi_i^{atm}$  and decorrelation-noise phase increment  $\Delta\phi_i^{noi}$ .

The investigation by Ferretti *et al.* (2000, 2001) indicated that if  $\Delta\phi_i^{res}$  is small enough, say  $|\Delta\phi_i^{res}| < \pi$ , both  $\Delta\varepsilon$  and  $\Delta v$  can be indeed derived directly from the  $M$  wrapped differential interferograms. In fact, the solution of  $\Delta\varepsilon$  and  $\Delta v$  can be obtained by maximizing the following objective function.

$$\gamma = \left| \frac{1}{M} \sum_{i=1}^M (\cos \Delta\phi_i^{res} + j \cdot \sin \Delta\phi_i^{res}) \right| = \text{maximum} \quad (3)$$

where  $\gamma$  = arc's model coherence (MC)

$$j = \sqrt{-1}$$

$\Delta\phi_i^{res}$  = difference between measurement and fitted value

Although the above objective function is highly nonlinear and the phase dataset is measured in a wrapped version, the two unknowns  $\Delta\varepsilon$  and  $\Delta v$  can be determined by searching a pre-defined solution space to maximize the MC value. It should be noted that the phase unwrapping can be avoided through the

process of function optimization, which is a really tough task in data processing of the conventional DInSAR.

### 3.2 Parameter Adjustment by LS Solution

With equation (3) we can compute the increments of elevation errors and linear deformation velocities along all the arcs in the network. By trials with simulated data, we have found that the arcs have an accurate solution for  $\Delta\epsilon$  and  $\Delta v$  if  $\gamma$  is larger than 0.45. The network can then be treated in a similar way as a leveling or GPS network; a weighted LS adjustment is applied to eliminate geometric inconsistency due to uncertainty in phase data, and thus obtaining the most probable values of the linear deformation velocities and elevation errors at PSs.

Taking the adjustment of LOS linear deformation velocities as an example, we present here some basic ideas for computation. A prototype observation equation for an arc is expressed as

$$\hat{v}_p - \hat{v}_l = \Delta v_{pl} + r_{pl}, \quad p \neq l, \forall p, l = 1, 2, K, K \quad (4)$$

where  $\hat{v}_p$  = linear deformation velocity at PS  $p$

$\hat{v}_l$  = linear deformation velocity at PS  $l$

$K$  = total number of all the PSs

Suppose there are  $Q$  arcs available in the network, we will have  $Q$  observation equations. The MC value of each arc can be used as a weight. With a weighted LS solution, the motion velocities at all the  $K$  PS can be eventually obtained. Such procedure can also be applied in a similar way onto the elevation-inconsistency network to estimate the elevation errors at all the  $K$  PSs. The Kriging interpolator can be applied to generate the deformation-velocity map and the elevation-error map.

As a remark, we underline that a reference point without motion or elevation error should be selected according to *a priori* information to obtain a unique solution with LS adjustment, and thus making all the estimates be related to the benchmark. In addition, we solved the large sparse matrix system using the software package termed UMFPACK (Davis, 2002). Moreover, it should be noted that the FCN used here is much stronger in terms of reliability than the TIN. Our simulation study shows that the LS solution derived with the FCN is much more accurate than that derived with the TIN even though a small portion of measurements ( $\Delta\epsilon$ ,  $\Delta v$ ) are intentionally set as outliers. This is because the redundancy number in the FCN is significantly larger than that in the TIN.

### 3.3 Separation of Nonlinear Deformation and Atmospheric Effect

The further analysis focuses on isolating nonlinear motion from atmospheric delay. For each interferometric pair, the residual phase increment (gradient) at each arc can be first derived. The integration of gradients (i.e., phase unwrapping) of all the arcs in the network is then performed by a weighted least squares method (Ghiglia & Pritt, 1998), and thus obtaining the residual phases in absolute sense at all the PS pixels for each pair. As mentioned before, the residual phase is contributed by nonlinear deformation, atmospheric delay and decorrelation noise.

It is possible to separate nonlinear motion from atmospheric

delay because the two terms have different spectral structure in space and time domain (Ferretti *et al.*, 2000; Mora *et al.*, 2003). In terms of atmospheric perturbation, a high correlation exhibits in space, but a significantly low correlation presents in time. In terms of nonlinear deformation, a strong correlation exists in space and a high correlation occurs in time. It is however not easy to discriminate the spectral bands between the nonlinear deformation and the atmospheric effect without availability of *a priori* information. Although an exact separation of the two terms is a challenged task, we try to achieve such purpose by introducing a strategy referred to as empirical mode decomposition (EMD) which was pioneered by Huang *et al.* (1998). This method is in principle different from the cascade filter applied by the previous studies (Ferretti *et al.*, 2000, 2001; Mora *et al.*, 2003).

To decouple signatures at each PS, we first estimate the time series of unwrapped residual phases corresponding to all the SAR acquisition times. This can be done using a singular value decomposition (SVD) method (for details, see Berardino *et al.*, 2002). The separation between atmospheric delay and nonlinear motion is then conducted by EMD using the time series of unwrapped residual phases.

The dataset being dealt with generally has several features: (a) the tens of samples are irregular; (b) the data is non-stationary (varying undulation); and (c) the data represents a nonlinear process. Theoretical study by Huang *et al.* (1998) indicated that the EMD approach is more advantageous for dealing with a nonlinear and nonstationary process than other signal analysis tools like Fourier transform. The EMD method separates the signal into a collection of intrinsic mode functions (IMF) that are useful for revealing some physical properties. For details of EMD operation, see Huang *et al.*, 1998.

By trials with real data, we can generally extract four IMFs from the time series of unwrapped residual phases. The IMFs with high frequencies correspond to atmospheric component, while the IMFs with low frequencies reflect nonlinear motion. It is not so direct to thoroughly discriminate them in the case of *no a priori* information available. However, reasonable results have been produced in our case when we consider the sum of the first and second level of IMFs as the atmospheric phases and treat the sum of the third and fourth level of IMFs as the nonlinear motions. The obtained two time series of phases for nonlinear motion and atmospheric delay at each PS are expressed as

$$\psi^{nldef}(t) = [\psi^{nldef}(t_0), \psi^{nldef}(t_1), \Lambda, \psi^{nldef}(t_N)] \quad (5)$$

$$\psi^{atm}(t) = [\psi^{atm}(t_0), \psi^{atm}(t_1), \Lambda, \psi^{atm}(t_N)] \quad (6)$$

where  $\psi^{nldef}(t_i)$  = phase for nonlinear motion at  $t_i$  (imaging time)

$\psi^{atm}(t_i)$  = phase for atmospheric delay at  $t_i$  (imaging time)

Finally, the total LOS deformation at any PS can be computed by summing the linear and nonlinear components, which can be written as a function of SAR acquisition time  $t_i$  by

$$def(t_i) = (t_i - t_0) \cdot \hat{v} + \frac{\lambda}{4\pi} \cdot \psi^{nldef}(t_i) \quad (7)$$

#### 4. DATSETS AND TESTING RESULTS

The western part of Phoenix (in Arizona, USA) consists of Deer Valley and the west Salt River Valley (Buckley, 2000), where several towns are included, i.e., Glendale, Peoria and Sun City. The excessive pumpage of groundwater in the areas has resulted in a large extent of land subsidence. The early interferometric study with a limited set of ERS C-band SAR images reported that several subsiding bowls exhibit across the towns (Buckley,

2000). We attempt to detect the spatio-temporal subsidence distribution in Phoenix by the method presented in section 2 and 3. For this study, we use 39 ERS SAR images acquired from 1992 to 2000, which are combined to form 86 interferometric pairs by thresholding of spatial and temporal baseline shorter than 120 m and 4 years, respectively. Table 1 lists the information of all the interferometric pairs. Figure 1 shows the study site and all the PSs superimposed onto the SAR amplitude image averaged from all the datasets.

Master/Slave Dates, YMD <sup>a</sup>	$B^{\perp}$ (m)	$T$ (days)	Master/Slave Dates, YMD	$B^{\perp}$ (m)	$T$ (days)	Master/Slave Dates, YMD	$B^{\perp}$ (m)	$T$ (days)
920710/930521	24	315	950827/960916	104	386	961230/970519	-35	140
920710/931008	-78	455	950827/980330	52	946	961230/981130	-86	700
920710/950827	-85	1143	950827/981130	88	1191	961230/990802	-65	945
920814/930205	-25	175	950827/990802	109	1436	961230/991220	-21	1085
920814/950514	80	1003	951105/951210	-68	35	961230/001030	54	1400
920814/960603	36	1389	951105/961021	106	351	970310/970519	-91	70
920918/951106	-79	1144	951106/951211	-51	35	970310/990315	73	735
920918/951210	64	1178	951106/980504	16	910	970310/991220	-76	1015
921023/960812	113	1389	951106/990628	-65	1330	970310/001030	-2	1330
930205/950514	105	828	951211/980504	67	875	970519/980330	-88	315
930205/960603	60	1214	951211/990628	-15	1295	970519/981130	-51	560
930521/931008	-101	140	960218/960219	53	1	970519/990802	-31	805
930521/950827	-109	828	960218/961021	-35	246	970519/991220	14	945
930521/960916	-5	1214	960218/980608	-5	841	970519/001030	89	1260
930521/961230	65	1319	960219/960428	87	69	980223/980713	90	140
930521/970519	31	1459	960219/961021	-88	245	980330/981130	37	245
930903/961230	-98	1214	960219/980608	-58	840	980330/990802	57	490
930903/970310	-42	1284	960603/980223	31	630	980330/991220	103	630
931008/950827	-8	688	960812/971215	-112	490	980504/990628	-81	420
931008/960812	-41	1039	960812/980330	85	595	980608/000508	13	700
931008/960916	97	1074	960916/961230	70	105	981130/990802	21	245
931217/960218	-73	793	960916/970519	36	245	981130/991220	65	385
931217/960219	-19	794	960916/980330	-52	560	990315/990524	50	70
931217/960428	68	863	960916/981130	-16	805	990315/001030	-75	595
931217/961021	-107	1039	960916/990802	5	1050	990524/990628	110	35
950514/960603	-44	386	960916/991220	50	1190	990802/991220	46	140
950514/980223	-13	1016	961021/980608	29	595	990802/001030	119	455
950514/980713	76	1156	961021/000508	42	1295	991220/001030	75	315
950827/960812	-33	351	961230/970310	56	70			

<sup>a</sup>YMD: year, month, day; Read 920710 as July 10, 1992, and 001030 as October 30, 2000.

Table 1. Summary information for 86 short baseline interferometric pairs

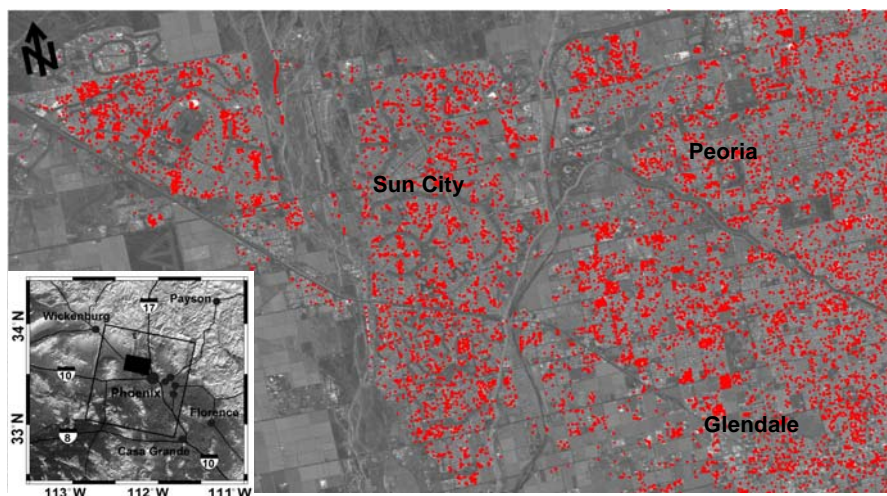


Figure 1. The study site and PS pixels superimposed onto the SAR amplitude image averaged from all the datasets.



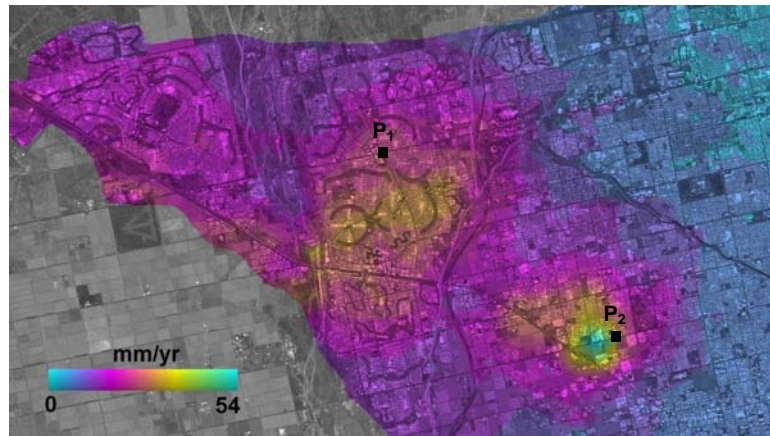


Figure 2. The subsidence-velocity map of the study area.  $P_1$  and  $P_2$  are marked as two PS points analyzed in Figure 4.

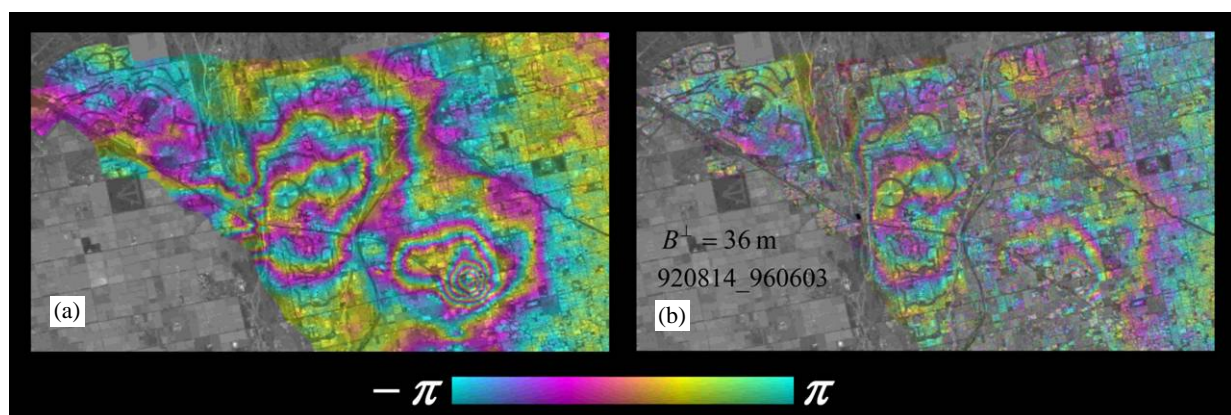


Figure 3. Comparison between simulated (a) and observed (b) differential interferograms with time interval of about 4 years.

The further data reduction concentrates on a patch of 27 km by 15 km within the ERS SAR frame as shown in Figure 1. The 14618 PS pixels detected out by ADI are superimposed onto the amplitude image by red points. 86 differential interferograms are generated by the “two-pass” method. The DEOS precise orbit state vectors and the SRTM DEM (about 10-m accuracy) are used to remove both flat-earth trend and topographic effect, thus highlighting land subsidence.

A very strong network was created by freely connecting each PS and all the others less than 1 km apart, resulting in 1463306 arcs. The increments of both linear motion velocities and elevation errors at each arc were then estimated by maximizing the model coherence with equation (3). The LOS deformation velocities and elevation errors at all the PSs are estimated by the weighted LS solution. Figure 2 reports the derived subsidence-velocity map in the study area. It can be seen that a subsiding bowl with a diameter of about 5 km appears in Glendale and has a peak subsidence rate of 54 mm/yr, while a wider subsiding bowl with a diameter of about 12 km spans Glendale, Peoria and Sun City and has a peak subsidence rate of 30 mm/yr. It can be inferred that the linear subsidence magnitude accumulated during the maximum time span of SAR acquisitions (about 8 years) may be up to 43 and 24 cm, respectively, at the two peaks. The eastern parts of the study site present subtle or zero subsidence. The subsidence in farmlands cannot be estimated due to the lack of PSs.

The fidelity of the estimated subsidence rates has been checked by visually comparing the observed differential interferograms

with those simulated using the subsidence-velocity map. As an example, Figure 3 shows such comparison for the differential interferograms with time interval of about 4 years. It is evident that they are in good agreement. Some minor inconsistency in some areas can be ascribed to atmospheric artifacts, topographic errors, and nonlinear motion. It also can be seen that the small-extent but deeper subsiding bowl in Glendale can be completely recovered by the PS networking method. However, its complete shape and extent do not present in any observed individual differential interferograms due to temporal decorrelation. All these not only verify that the estimation approach is powerful and reliable, but also suggest that the linear subsidence in the study area dominates the nonlinear component.

The nonlinear subsidence was separated from the atmospheric artifacts by both the SVD and EMD method. As examples, Figure 3 shows the temporal evolution of atmospheric delay in LOS direction, nonlinear and total subsidence at two PS points ( $P_1$  and  $P_2$ ) near the centres of two subsiding bowls (see Figure 2). The atmospheric variation is evidently random in time. The atmospheric artifacts at  $P_2$  range from -2.0 to 2.1 cm, which are slightly higher than those at  $P_1$ . Point  $P_2$  presents a dynamic range of -2.5–2.2 cm nonlinear subsidence, while point  $P_1$  has a narrower range of nonlinear subsidence (-2.0–1.4 cm). Additionally, it can be seen that point  $P_1$  located near the deeper subsiding bowl exhibits more seasonal undulation than point  $P_2$  located near the shallow subsiding bowl. From the two profiles of total subsidence, we stress once again that the linear trend of subsidence dominates the nonlinear component in this study area.

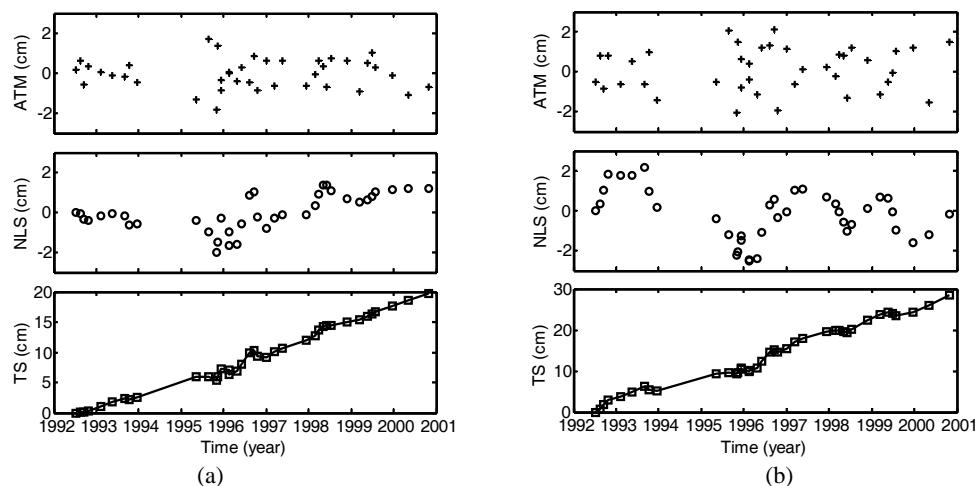


Figure 4. Temporal variation of atmospheric (ATM) delay in LOS direction, nonlinear subsidence (NLS) and total subsidence (TS) at two PS points as marked in Figure 2. (a): for  $P_1$  and (b) for  $P_2$ .

## 5. CONCLUSIONS

Combining merits of both PS and SBAS technique, this paper presents a PS-networking approach to map ground deformation with time series of SAR images. Data modelling and parameter (e.g., deformation velocity) estimating by function optimization and LS solution rely on the freely-connected network that may mitigate the negative impacts of both decorrelation noise and atmospheric delay. In terms of reliability, such FCN is more advantageous than the TIN applied elsewhere. Both SVD and EMD tool can be successively employed to reasonably isolate nonlinear deformation from atmospheric delay. For algorithm validation, some experiments have been performed to analyze historical evolution of subsidence in Phoenix with 39 ERS SAR images. The testing results show that such PS-networking approach is viable and efficient for detecting of the temporal behaviour of ground deformations.

## REFERENCES

- Berardino, P., G. Fornaro, R. Lanari, E. Sansosti, 2002. A new algorithm for surface deformation monitoring based on small baseline differential SAR interferograms. *IEEE Trans. Geosci. Remote Sens.*, 40(11), pp. 2375-2383.
- Buckley, S.M., 2000. Radar Interferometry Measurement of Land Subsidence. Ph.D. thesis, The University of Texas at Austin, Texas, USA.
- Davis, T.A., 2002. UMFPACK Version 4.0 User Guide. <http://www.cise.ufl.edu/research/sparse/umfpack/v4.0/UserGuide.pdf>. (accessed 16 Mar. 2006)
- Ding, X.L., G.X. Liu, Z.W. Li, Y.Q. Chen, 2004. Ground subsidence monitoring in Hong Kong with satellite SAR interferometry. *PE&RS*, 70(10), pp. 1151-1156.
- Ferretti, A., C. Prati, F. Rocca, 2000. Nonlinear subsidence rate estimation using permanent scatterers in differential SAR interferometry. *IEEE Trans. Geosci. Remote Sens.*, 38(5), pp. 2202-2212.
- Ferretti, A., C. Prati, F. Rocca, 2001. Permanent scatterers in SAR interferometry. *IEEE Trans. Geosci. Remote Sens.*, 39(1), pp. 8-20.
- Ghiglia, D. C. and M. D. Pritt, 1998. *Two-Dimensional Phase Unwrapping: Theory, Algorithms, and Software*. John Wiley & Sons, Inc, New York, pp. 178-277.
- Huang, N. E., Z. Shen, S. R. Long, M. L. Wu, H. H. Shih, Q. Zheng, N. C. Yen, C. C. Tung and H. H. Liu, 1998. The empirical mode decomposition and Hilbert spectrum for nonlinear and nonstationary time series analysis. *Proceedings of the Royal Society of London (Series A)*, 454, pp. 903-995.
- Liu, G. X., 2003. Mapping of Earth Deformations with Satellite Radar Interferometry: A Study of Its Accuracy and Reliability Performances. Ph.D. dissertation, The Hong Kong Polytechnic University, Hong Kong, China.
- Lyons, S. and D. Sandwell, 2003. Fault creep along the southern San Andreas from InSAR, permanent scatterers, and stacking. *JGR*, 108(B1), pp. 2047-2070.
- Mora, O., J. J. Mallorqui and A. Broquetas, 2003. Linear and nonlinear terrain deformation maps from a reduced set of interferometric SAR images. *IEEE Trans. Geosci. Remote Sens.*, 41(10), pp. 2243-2253.
- Sandwell, D. T. and E. J. Price, 1998. Phase gradient approach to stacking interferograms. *JGR*, 103(B12), pp. 30183-30204.
- Zebker, H.A., J. Villaseno, 1992. Decorrelation in interferometric radar echoes. *IEEE Trans. Geosci. Remote Sens.*, 30(5), pp. 950-959.

## ACKNOWLEDGEMENTS

The work presented here was partially supported by two grants from the National Natural Science Foundation of China (Project No. 40774004, 40374003). The research was performed while the first author was a visitor to Dr. S. M. Buckley at Centre for Space Research, The University of Texas at Austin. The authors would like to thank ESA and USGS for providing radar data and SRTM DEM, respectively, as well as the Delft University of Technology for providing the precise orbital data. They also thank Mr. D. Yang for his assistance on SAR data processing.